Meanders and eddies formation by a buoyant coastal current flowing over a sloping topography

Laura Cimoli[1,3], Alexandre Stegner[2], and Guillaume Roullet[3]

[1]University of Brest, CNRS, IRD, Ifremer, Laboratoire d'Océanographie Physique et Spatiale, IUEM, Brest, France
[2]Laboratoire de Météorologie Dynamique, CNRS/École Polytechnique/Université Paris-Saclay, Palaiseau, France
[3]Department of Physics, University of Oxford, Oxford, United Kingdom

Correspondence to: Laura Cimoli (laura.cimoli@physics.ox.ac.uk)

Abstract. This study investigates the linear and non-linear instability of a buoyant coastal current flowing along a sloping topography. In fact, the bathymetry strongly impacts the formation of meanders or eddies and leads to different dynamical regimes that can both enhance or prevent the cross-shore transport. We use the Regional Ocean Modeling System (ROMS) to run simulations in an idealized channel configuration, using a fixed coastal current structure and testing its unstable evolution

5 for various depths and topographic slopes. The experiments are integrated beyond the linear stage of the instability, since our focus is on the non-linear end state, namely the formation of coastal eddies or meanders, to classify the dynamical regimes. We find three non-linear end states, whose properties cannot be deduced solely from the linear instability analysis. They correspond to a quasi-stable coastal current, the propagation of coastal meanders, and the formation of coherent eddies. We show that the topographic parameter, T_p, defined as the ratio of the topographic Rossby wave speed over the current speed, plays a key role

10 in controlling the amplitude of the unstable cross-shore perturbations. This result emphasizes the limitations of linear stability analysis to predict the formation of coastal eddies, because it does not account for the non-linear saturation of the cross-shore perturbations, which is predominant for large negative T_p values. We show that a second dimensionless parameter, the vertical aspect ratio γ, controls the transition from meanders to coherent eddies.

We suggest the use of the parameter space (T_p, γ) to describe the emergence of coastal eddies or meanders from an unstable

15 buoyant current. By knowing the values of T_p and γ for an observed flow, which can be calculated from hydrological sections, we can identify which non-linear end states characterizes that flow, namely if it is quasi-stable, meanders, or forms eddies.

1   Introduction

Coastal currents can act either as a source of coherent eddies or as a dynamical barrier to the offshore redistribution of coastal waters, thus controlling the cross-shelf tranport in a local or regional circulation. When these currents are unstable, large

20 meanders grow and can lead to the formation of meso-scale eddies that capture and transport water masses towards the open sea over large stretches of the coastline. Conversely, stable coastal currents enhance the along shore transport and strongly reduce, or even prevent, the cross-shelf transport. Hence, the formation and the propagation of coastal eddies across the coastal shelf play a significant role in the local mixing of biogeochemical properties, in the dispersion of pollutants, and in the redistribution of nutrient-rich coastal waters toward the oligotrophic open sea (Riandey et al., 2005).

On the one hand, many coastal currents such as the Algerian Current (Millot, 1999; Obaton et al., 2000; Puillat et al., 2002), the West Greenland Current (Eden and Boning, 2002; Pickart et al., 2005; Hátún et al., 2007), and the Norwegian Coastal Current (Björk et al., 2001) shed coherent and long-lived eddies off the coast. On the other hand some coastal flows, such as the Bransfield Current (Savidge and Amft, 2009; Sangrá et al., 2011; Poulin et al., 2014) or the Northern Current in the

5 western Mediterranean Sea (Sammari et al., 1995; Millot, 1999; Birol et al., 2010) appear to be quasi-stationary along the shelf slope. Hence, the impact of a sloping bathymetry on the development and the evolution of meanders and eddies has been topic of several studies. The first studies were devoted to the linear stability of coastal flows, while the most recent numerical simulations focus on the non-linear formation of meso- and submeso-scale eddies from shelf/slope density fronts or currents (Pennel et al., 2012; Stewart and Thompson, 2013; Gula et al., 2014).

10 There exist numerous linear stability analyses of baroclinic currents flowing over sloping topography which are based on layered models (Mysak, 1977; Mysak et al., 1981; Gula and Zeitlin, 2014; Poulin et al., 2014) or continuous stratification (Blumsack and Gierasch, 1972; Mechoso, 1980; Lozier et al., 2002; Lozier and Reed, 2005; Isachsen, 2011). In the framework of quasi-geostrophic (QG) models, both the two-layer model and the continuously stratified Eady model show that when the isopycnals and the topographic slopes tilt in opposite directions, a sloping topography reduces the growth rate of baroclinic

15 modes with respect to a flat bottom case. These idealized stability analysis demonstrate that the central parameter of the problem is not the bottom slope (s), but the ratio of the bottom slope over the isopycnal slope (α), defined as the *topographic parameter*. This ratio, $T_0 = s/\alpha$, is, by convention, negative when the shelf and the isopycnals tilt in the opposite sense. Poulin et al. (2014) extend these analyses to a two-layer, shallow-water framework, and show that, as for the QG models, the increase of the bottom slope tends to stabilize the baroclinically unstable modes. They also show that, when the structure of the coastal

20 jet allows for both baroclinic and barotropic instabilities, the stabilization of the baroclinic modes leads to the dominance of the barotropic horizontal shear instability.

Hence, for a geostrophic coastal current, the linear stability analysis predicts that two different regimes of instability with distinct wavelength selection can occur above the shelf bathymetry. When the geostrophic coastal current is controlled by the baroclinic instability, the decrease of the topographic parameter T_0 (with $T_0 < 0$) yields a selection of smaller unstable

25 wavelengths, which can be two or three times smaller than the one emerging in a flat bottom configuration. However, for more negative values of T_0, the growth rates of baroclinic modes decreases strongly and the horizontal shear instability becomes dominant. The latter is then weakly affected by the shelf slope and leads to large unstable wavelengths (Poulin et al., 2014).

However, it is well known that the linear stability analysis is limited by its inability to predict the final amplitude of unstable meanders. Further non-linear processes may lead to larger or smaller structures than the ones predicted by the linear analysis.

30 Moreover, previous studies have shown that a sloping topography has a strong impact on the non-linear saturation of unstable surface flows (Sutyrin, 2001). Experimental studies (using a two-layer stratification) of coastal fronts or coastal currents over linear shelf slopes (Pennel et al., 2012; Geheniau et al., 2016) have shown that there are no large meanders or any eddy detachments when the topographic parameter reaches values below $T_0 \simeq -3$. This is evidence that the non-linear saturation of the linear instability becomes important when the topographic slopes are comparable to the isopycnal slopes.

The primary goal of this study is to go beyond the linear stability analysis and investigate the non-linear impact of the sloping topography on the formation of coastal eddies, namely whether or not the current generates a significant non-linear cross-shore disturbance. To answer this question, we use an idealized model of a buoyant current with a continuous and non-uniform stratification. Indeed, the effects of a continuous stratification and the relevent set of dynamical parameters that govern

5 the stability of geostrophic currents along a sloping bathymetry are not well established. Unlike standard linear instability analysis, the use of a full non-linear model allows us to discuss the end state of the instability, in other words the various regimes of formation of large-scale meanders or coastal eddies. We find that investigating the non-linear evolution shows three possible non-linear end states, while the linear analysis predicts only two types of instability - barotropic and baroclinic. A classification of the various non-linear end states provides a more direct comparison with surface oceanic observations, such

10 as SST images or SSH maps, where only finite amplitude perturbations or coherent eddies can be detected.

In section 2, we present the initial state of the coastal current and the main dynamic and topographic parameters of the system. In section 3, we investigate how different values of the bottom slope and depth affect the stability of a surface intensified current. We then show, in section 4, the role played by the topographic parameter in controlling the amplitude of the unstable perturbations. If these perturbations reach a finite amplitude large meanders or coherent eddies are formed. The characteristics

15 of these final non-linear structures and their corresponding parameter space are given in the section 5 and 6. Discussions and conclusions are given in the final section 7.

2   Numerical model setup

To investigate the effect of a sloping topography on meanders and eddy formation in a buoyant coastal current, we employ the Agrif version (Penven et al., 2006; Debreu et al., 2011) of the Regional Oceanic Modeling System (ROMS) (Shchepetkin and

20 McWilliams, 2003, 2005). While keeping the model setup idealized, our configuration has been built with a particular observed ocean current system in mind, namely the Bransfield Current in Antarctica. This decision stems from our original motivation of extending the analysis made with a two-layer, shallow-water model presented in Poulin et al. (2014) to a continuously stratified, 3D primitive equations model.

We use a periodic rectangular domain, with x as the along-shore axis, y the cross-shore axis (positive offshore), and z

25 the vertical axis (the model uses terrain-following vertical coordinates). Two distinct grid resolutions are used, a coarse grid resolution ($dx = dy = 2$ km and $N = 32$ sigma vertical levels) and a higher resolution grid ($dx = dy = 0.6$ km and $N = 32$ sigma vertical levels). Most of the results presented here come from the low resolution runs, but we found a good convergence of the higher resolution simulations for various dynamical regimes identified. The horizontal domain dimensions are $L_x = 256$ km, and $L_y = 160$ km, respectively. This configuration corresponds to a coastal channel with periodic boundary conditions for

30 the along-shore direction, and free slip boundaries at the coast ($y = 0$) and offshore ($y = L_y$). The effect of the bottom friction is here neglected by setting it to zero, since the focus of this paper is on the inviscid dynamics and a non-zero bottom friction would slow down the current during the initial period of integration.

The initial state consists of a steady geostrophic surface current flowing along an idealized sloping bathymetry (figure 1a). The water depth, at a given distance y from the coast, is given by a hyperbolic tangent profile:

$$h(y) = H + \Delta h \tanh\left[s\left(y - L_s\right)/\Delta h\right], \tag{1}$$

where H is water depth below the maximum current velocity, Δh the height amplitude, L_s the pivotal distance and s the
5 maximal shelf slope (figure 1a). Throughout this study we keep $L_s = 10$ km and $\Delta h = 600$ m constant, while we vary both H and s. This profile has been often used as a generic bathymetry in previous works (Lozier et al., 2002; Lozier and Reed, 2005; Poulin and Flierl, 2005; Stewart and Thompson, 2013), and according to Poulin et al. (2014), the hyperbolic tangent profile fits remarkably well the shelf bathymetry in the Bransfield Strait, from which the numerical setup of this work takes inspiration.

We use a linear equation of state and set salinity to a constant; thus, the density stratification is a function of temperature
10 only and is equal to $\rho = -\rho_0 \, \alpha_T \, T$. The thermal stratification for the unperturbed ocean is defined by the following function:

$$T_{oc} = T_0 + \frac{N_0^2}{g\,\alpha_T} z + \Delta T \, \tanh(z/H_T), \tag{2}$$

where N_0 ($\simeq 2.4$ x $10^{-4} \, s^{-1}$) is a minimal Brunt-Väisälä frequency in the deep layer, $\Delta T = 2°$C is the temperature difference between the surface and the deep ocean, g is the gravitational acceleration and α_T is the thermal expansion coefficient of seawater ($\alpha_T = \partial_T \rho/\rho_0 \simeq 2.8$ x $10^{-4} \, K^{-1}$). Hence, the relative Brunt-Väisälä frequency varies from $N_s/f = 40$ at the surface
15 to $N_0/f \simeq 2$ at the bottom (figure 1b). The typical unperturbed thermocline depth is set here at $H_T = 200$ m. The coastal current, in thermal wind balance, is driven by a warm temperature anomaly above the shelf, that we define as

$$T_{an}(y, z) = \Delta T_{jet} F(y) \, G(z),$$
$$F(y) = 1 - \tfrac{1}{2}\left[1 + \tanh\left(\tfrac{y-D}{L}\right)\right] \tanh^2(1.2\,y/D), \tag{3}$$
$$G(z) = \exp(-z^2/2\,H_{jet}^2).$$

The width and the depth of the coastal jet are fixed by $L = 10$ km and $H_{jet} = 250$ m, respectively. D is the distance to the coast, and in all our analysis we use $D = L = L_s = 10$ km. The temperature difference ΔT_{jet} is determined indirectly from
20 the maximum jet velocity U_{max}, obtained upon vertical integration of the thermal wind balance

$$\partial_z U(y, z) = \frac{g}{f}\partial_y\rho = -\frac{\alpha_T \rho_0}{f} G(z)\partial_y F(y), \tag{4}$$

assuming $U = 0$ at $z = H + \Delta h$, i.e. over the flat part of the domain, and where the Coriolis parameter $f = 1.26$ x $10^{-4} \, s^{-1}$ is constant. The surface velocity $U_0(y) = U(y, z = 0)$ is then proportional to $\partial_y F(y)$, and is thus quite similar to the linear gaussian jet used by Poulin et al. (2014) to model the Bransfield Current. The velocity section in the vertical plane (figure 1)
25 shows a surface intensified current with very low values in the deep layer below $H_{jet} = 250$ m.

The model solves the primitive equations with a split-explicit free-surface, where short time steps are used to advance the surface elevation and barotropic momentum equation, and a larger time step is used for temperature and baroclinic momentum. We stick to the ROMS philosophy of removing explicit horizontal turbulent closure terms on both temperature (no diffusion)
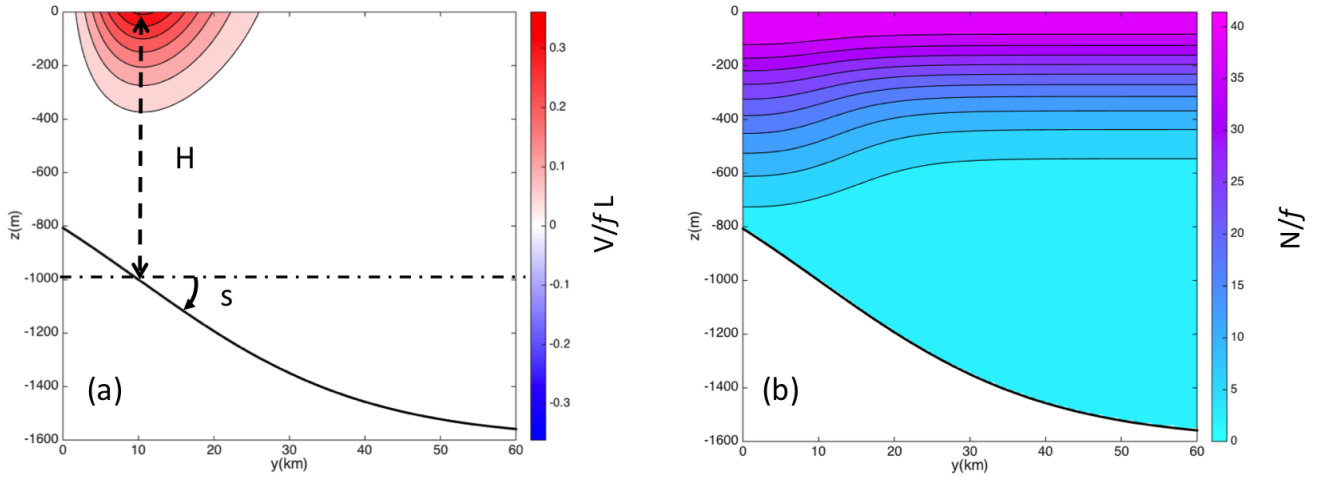
Figure 1. Simplified configuration of a surface coastal current above an hyberbolic tangent bathymetry. The along shore velocity (left panel) and the Brunt Väisälä frequencies (right panel) are plotted in dimensionless form (V/fL, N/f) and correspond to the configuration where $H = 1000$ m, $L = 10$ km, $s = 3\%$, $\Delta T_{jet} = 0.8°$C, $U_{max} = 35$ cm s^{-1}, $f = 1.26$ x 10^{-4} s^{-1}.

and momentum (no viscosity), and of letting the third order upstream-biased advection operator handle the necessary dissipation at grid-scale. We consider initial value problems with no external forcing, but only an initial white noise added on the velocity field. Consequently the surface momentum, heat, and freshwater fluxes are set to zero.

2.1 Dynamic and topographic parameter

5 For a flat bottom configuration, the dynamics of the coastal current mainly depend on the Rossby (Ro) and the Burger (Bu) numbers:

$$Ro = \frac{U_{max}}{f\,L}\,, \qquad\qquad Bu = \left(\frac{R_d}{L}\right)^2, \qquad\qquad (5)$$

where R_d is the first baroclinic deformation radius. We compute the linear eigenmodes and the corresponding deformation radius R_d of the vertical stratification $\rho(y = D, z)$ at the location of the maximum current velocity U_{max}, that is for a depth

10 H. The standard eigenmode equation and the typical structure of the first baroclinic mode are given in the Appendix A. The typical values for the first baroclinic deformation radius range between $R_d \simeq 5$ km and $R_d \simeq 7$ km, leading to small Burger numbers, $Bu = 0.25 - 0.5$. Thus, the available potential energy of the initial flow is higher than its kinetic energy.

In this study the intensity of the initial current is kept fixed with a maximum surface velocity $U_{max} = 35$ cm s^{-1}. The corresponding Rossby number is then $Ro = U_{max}/(fL) = 0.25$ and the anticyclonic (cyclonic) vorticities maximum values

15 are $\zeta_{min}/f \simeq -0.35$ ($\zeta_{max}/f \simeq 0.2$). The relative vorticity never goes below the threshold $\zeta/f = -1$ of inertial instability

(Knox, 2003; Plougonven and Zeitlin, 2009). Hence, at the first order of approximation, the dynamical evolution of the coastal current satisfies geostrophic balance.

To establish a contact point with two-layer theories, we introduce the vertical aspect ratio parameter:

$$\gamma = \frac{H_{jet}}{H - H_{jet}}, \tag{6}$$

5 where H_{jet} is the thickness of the upper layer, encompassing the surface intensified jet, and $H - H_{jet}$ is the thickness of the lower layer, almost at rest. This parameter is the close equivalent of the two layer ratio parameter $\gamma_2 = H_1/H_2$ that controls the baroclinic instability in the standard QG Phillips model with unequal layer thicknesses (Phillips, 1954; Pedlosky, 1987; Vallis, 2006). For a flat bottom configuration, the largest growth rates are found when $\gamma_2 = 1$ and the baroclinic growth rate vanishes when γ_2 tends towards zero (Poulin et al., 2014). Hence, if we consider a continuously stratified flow above a flat

10 bottom ($s = 0$) and if we keep Ro and Bu constant, the geostrophic instabilities of the surface current will then be controlled by the single parameter left, namely γ.

This is not the case in a sloping topography scenario. In fact, since the current flows above a sloping bathymetry, a key dynamical feature is the interaction of the current with the topographic Rossby waves. In the case of a buoyant coastal current, the topographic Rossby waves propagate in the same direction as the flow. The propagation speed of these waves is proportional to

15 the dimensionless topographic slope s. Previous studies, using the continuously stratified Eady model (Blumsack and Gierasch, 1972; Mechoso, 1980; Isachsen, 2011), have shown that the ratio of the bottom slope (s) over the isopycnal slope (α) is the relevant topographic parameter of the problem. However, in our case there is no such definite unique value for the isopycnal slope because isopycnals are bent and so their slopes vary with depth. Therefore, we define a topographic parameter, T_p, as the ratio of the characteristic speed of topographic Rossby waves, U_{TRW}, over the maximum speed of the surface current:

20 $$T_p = \frac{U_{TRW}}{U_{max}} = -\frac{s f R_d^2}{H U_{max}}. \tag{7}$$

The speed $U_{TRW} = -sf/(Hk^2) = -sfR_d^2/H$ corresponds here to a characteristic phase speed of topographic Rossby waves, with a typical scale $kR_d = 1$. This topographic parameter can also be written in terms of a *topographic beta* parameter $\beta_t = -sf/H$, as:

$$T_p = \frac{\beta_t R_d^2}{U_{max}}. \tag{8}$$

25 We will see later that T_p, including information both of the topographic slope (s) and the depth (H), is the key parameter that controls the non-linear saturation of the coastal current, namely the formation of meanders and eddies that enhance the cross-shore transport.

3 The effect of variable topographic slope (s) and depth (H)

In this chapter we present how different slopes and bottom depths can affect the growth rate and the non-linear saturation of

30 the cross-shore perturbations, while keeping all the other parameters and the buoyant current constant.

At the initial stage the coastal current is mainly along-shore, hence we can assume that $V \ll U$, namely the cross-shore velocity, V, is much smaller than the along-shore velocity, U. Therefore, the growth of the cross-shore velocity V is directly proportional to the growth of unstable perturbations that induce a cross-shore transport. Hence, in order to study both the exponential growth and the non-linear amplitude of these perturbations, we calculate at each time step the domain-integrated

5 ratio:

$$R(t) = 2\frac{KE_y}{KE} = 2\frac{<V^2>}{<U^2 + V^2>}, \qquad (9)$$

where the total kinetic energy KE is the sum of the cross-shore (KE_y) and the along-shore (KE_x) contributions to the kinetic energy, and $<>$ is the domain integration. The factor of 2 in equation (9) has been inserted so that the ratio on the left-hand side approaches 1 as the along-shore and cross-shore contributions to the KE approach parity.

10 Various metrics could be used to quantify the departure from the inital coastal current. We note here that, while this analysis does not take into account any anisotropic perturbation directed in the along-shore direction, we have checked that this does not change qualitatively the results presented in this study. Moreover, the focus here is on the generation of cross-shore transport by an unstable coastal current, as opposed to a stable along-shore flow that prevents the transport of water offshore. Therefore, we chose this metric to put emphasis on the cross-shore perturbations that may break the along-shore jet and lead to the formation

15 of large meanders or coherent eddies.

The temporal evolution of the ratio in equation (9) is plotted in figure 2, which shows that the cross-shore contribution of the kinetic energy is, at the initial stage, at least one order of magnitude smaller than the along-shore one: $KE_y \ll KE_x(t=0) \simeq KE(t=0)$. These weak cross-shore motions are due to the initial white noise introduced in the numerical simulations. This initial noise is added only on the velocity field, hence the geostrophic adjustment of this initial unbalance field leads to a decay

20 of KE_y/KE during the first days of the simulations. Then, an exponential growth of the above ratio occurs due to the linear instability of the coastal current. As long as the amplitude of the unstable perturbations remains small (i.e. $KE_y \ll KE$), we can quantify the mean growth rates of the instability from the log-linear plot. If we assume that the amplitude of the most unstable mode is proportional to the cross-shore velocity, we can deduce the maximal unstable growth rate σ_m from the slopes of the log-linear plot, as shown from the solid lines in figure 2b. The slope returns the exponential growth $2\sigma_m$ of KE_y. When

25 the unstable currents start to form large meanders or when the detachment of coherent eddies occurs, an equipartition between the cross-shore and the along-shore contributions to the kinetic energy is reached, regardless of the intensity of the eddies. Consequently, the *non-linear saturation* parameter, namely the temporal maximum of the ratio $R(t)$,

$$\varepsilon = \max(R(t)) = \max(2KE_y/KE), \qquad (10)$$

tends to a value close to unity. We stress here that what we call the non-linear saturation parameter returns only the saturation

30 of the cross-shore perturbations, and does not take into account the along-shore perturbations (that never reach finite amplitude values). Similar analyses were performed by Pennel et al. (2012) and Geheniau et al. (2016) using the surface kinetic energy because only the surface velocity field, derived with a good accuracy from particle image velocimetry (PIV), is available in laboratory experiments.
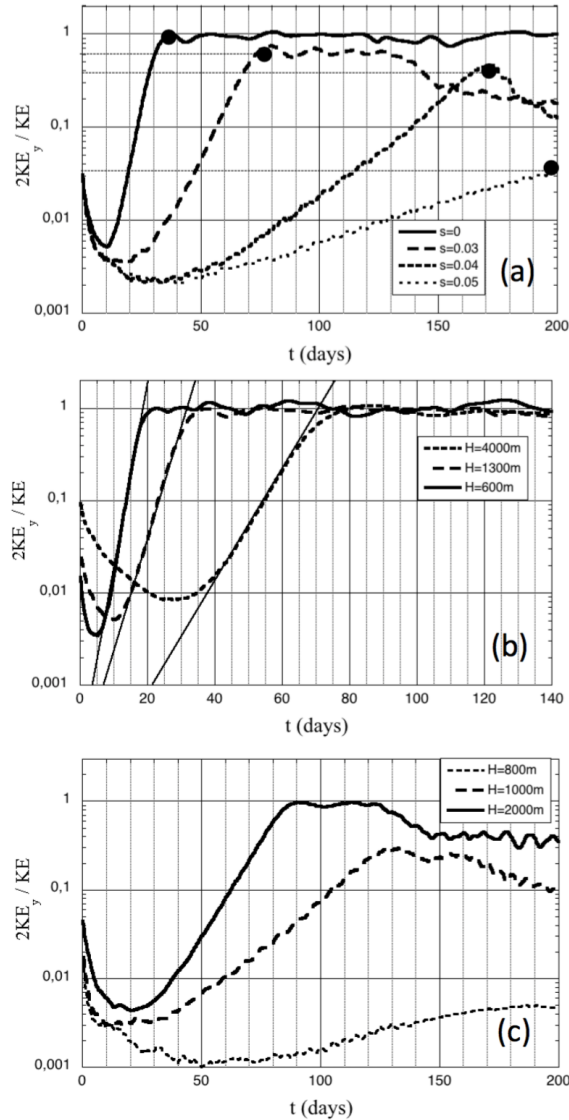
Figure 2. Time evolution of $R(t) = 2\,KE_y/KE$. In the upper panel (a) the depth $H = 1300$ m is kept constant while the shelf slope varies $s = 0, 3\%, 4\%, 5\%$. The central panel (b) corresponds to the the flat bottom configuration ($s = 0$) for various depth $H = 600$ m, 1300 m, 4000 m. In the bottom panel (c) the shelf slope $s = 3\%$ is kept constant while the depth varies $H = 800$ m, 1000 m, 2000 m.

We now present the impact that a variable s and/or H have on the growth rate of the instabilities of a buoyant current.

Figure 2a shows that, while keeping a constant water depth H, the unstable growth rate decreases as we increase the bathymetric slope. This is expected, since previous studies have shown that a steep shelf slope reduces the unstable growth of baroclinic modes (both with a two-layer model (Mysak, 1977; Mechoso, 1980; Poulin et al., 2014; Gula and Zeitlin, 2014)

and the continuously stratified Eady model (Blumsack and Gierasch, 1972; Mechoso, 1980; Isachsen, 2011)). However, these linear stability analyses can predict neither the non-linear evolution of the unstable perturbations nor the final state of the system. It is only recently that laboratory experiments with a two-layer stratification (Geheniau et al., 2016), have shown that the level of the non-linear saturation (i.e. the saturation parameter ε) could be significantly smaller if the topographic parameter

5 $T_0 = s/\alpha < 0$ reaches finite values, namely if the shelf slope is steep enough. Here, we confirm this behaviour for a continuously stratified coastal current. According to figure 2a, the saturation parameter (solid circles) decreases from $\varepsilon = 0.74$, to $\varepsilon = 0.45$ and $\varepsilon = 0.034$ when the shelf slope increases from $s = 3\,\%$, to $s = 4\,\%$ and $s = 5\,\%$, respectively.

Now, we analyse the cases of a constant slope s and a variable H. For the flat bottom configuration ($s = 0$), when the water depth H increases, the growth rate σ_m decreases (figure 2b). For the simplified two-layer QG Phillips model (Pedlosky, 1987;

10 Vallis, 2006), it is well known that the growth rates of baroclinic perturbations are mainly controlled by the vertical aspect ratio parameter $\gamma_2 = H_1/H_2$. The largest growth rates are found when $\gamma_2 = 1$. When γ_2 is reduced, say by increasing the lower layer thickness H_2, both the growth rate and the most unstable wavenumber decrease. We found a similar behaviour for the continuously stratified configuration. Keeping a constant jet depth H_{jet} and increasing the bottom depth H yields a slower instability of the surface coastal current. Nevertheless, we found that with a flat bottom the unstable perturbations always reach

15 a finite amplitude ($\varepsilon \simeq 1$).

A similar agreement with the two-layer case is found when we vary the water depth above a sloping bathymetry: as we reduce H, we get a stronger stabilization of the surface current. According to the Figure 2c, both the linear growth rate σ_m and the non-linear saturation parameter ε decrease when the water depth H is decreased while keeping the bottom slope constant at $s = 3\,\%$. Indeed, for this specific bottom slope, when $H = 2000$ m the unstable cross-shore perturbations lead to finite

20 meanders or coastal eddies ($\varepsilon \simeq 1$) while only very weak cross-shore fluctuations could grow ($\varepsilon \simeq 0.05$) when $H = 800$ m.

This initial set of results suggest that both the bottom slope and the water depth have a strong impact on the non-linear stabilization of the along-shore current. The impact of the sloping bathymetry is increased when the water depth is reduced, and inversely for very large water depths. Extrapolating this to the case of an infinitely deep ocean, we could expect to reduce or even cancel the impact of the bottom slope. The combined effect of variable s and H is described in the following section,

25 where we analyse different quantities with respect to the topographic parameter, which provides a useful re-scaling of the wide range of cases that we have studied (see Table 1).

4 The role of the topographic parameter T_p

In order to quantify more precisely the influence of a sloping bathymetry on the stability of the coastal current, we plot in figure 3a the dimensionless growth rates as a function of the topographic parameter T_p. Each experiment on figure 3 is labelled

30 with either s or H indicating that the companion parameter (H or s, respectively) is varied. Hence, the points with $H = 950$ m spans s in [0 4%], which corresponds to T_p in [-0.5 0] (see Table 1).

Figure 3a shows that for negative values below $T_p \simeq -0.3$, the growth rates of the unstable perturbations decrease towards a relatively small value $\sigma_m R_d/V_{max} \simeq 10^{-3}$, which is one order of magnitude smaller than unstable growth rates in the flat
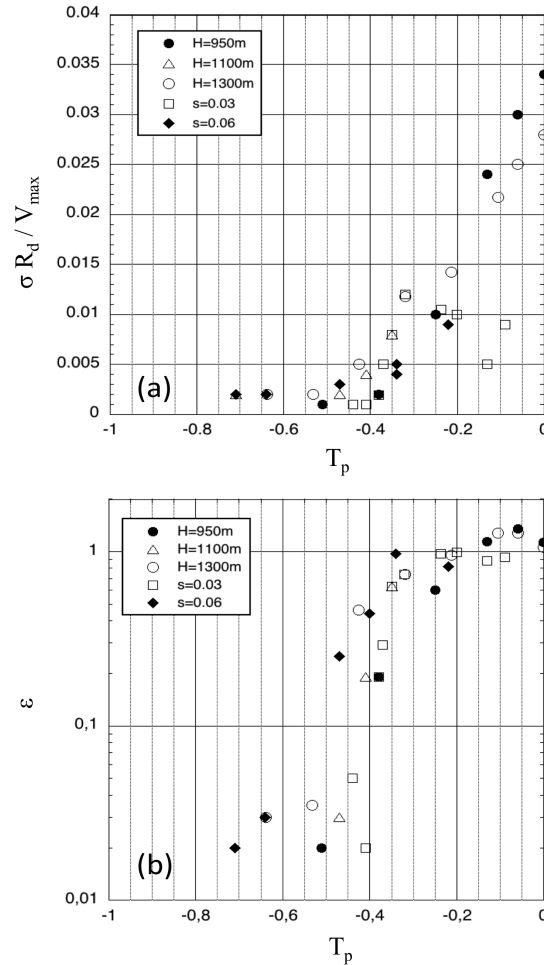
Figure 3. (a) Dimensionless growth rates $\sigma_m R_d/V_{max}$ and (b) the non-linear saturation parameter ε as a function of the topographic parameter T_p for the same coastal current ($Ro = 0.25$) above various shelves. We consider here a large range of bottom slopes ($s = 0 - 6\,\%$) and water depths ($H = 600 - 5000$ m).

bottom cases ($T_p = 0$). However, for intermediate values of the topographic parameter ($-0.3 < T_p < 0$), two distinct branches are visible in figure 3a. When T_p decreases, the growth rate of the upper branch decreases linearly with T_p, whereas the growth rate of the lower branch slightly increases with decreasing T_p until it merges with the upper branch. This behaviour suggests the possible existence of two distinct modes of instability for the same value of T_p.

5   As it was shown in Poulin et al. (2014), an efficient way to identify distinct unstable modes is to study the evolution of the most unstable wavelength λ_m (or wavenumber k_m, where $k_m = 2\pi/\lambda_m$) as a function of the relative slope parameter, which is T_p in our continuously stratified case.

In order to estimate the most unstable wavenumber, we perform, as in Pennel et al. (2012), a Fourier decomposition of the cross-shore velocity at the surface ($z = 0$). We then select the unstable mode k_m that both follows an exponential growth and reaches the highest amplitude. In few cases, a first mode grows and saturates at a given amplitude while a second one, having similar growth rate, saturates at a higher level after a while. For these specific cases we plot the two wavenumbers in

5   figure 4. We clearly see, in this figure, two distinct branches. For the upper one, the unstable wavenumber $k_m R_d$ increases (i.e. λ_m decreases) when the topographic parameter decreases until the limit value $T_p \simeq -0.4$ is reached. Below this value, the upper branch does not exist because its growth rate becomes smaller than the one of the lower branch, therefore this mode does not emerge during the time integration. For the lower branch, the most unstable wavenumber is both smaller and much less impacted by the variation of the topographic parameter, suggesting that this mode corresponds to a barotropic mode, as

10   we will soon show. In order to identify the nature of these two branches we determine the source of kinetic energy of the perturbations for the instability. In this simplified jet configuration, there are basically two source terms (Gula et al., 2015): $< w'b' >$, the extraction from the potential energy of the jet, and $< -u'v'\partial_y U >$, the extraction from the horizontal shear, where $u' = U - \overline{U}$, $v' = V - \overline{V}$ and $w' = W - \overline{W}$ are the velocity perturbations to the along-shore averaged velocities, and $\overline{U}$, $\overline{V}$, and $\overline{W}$ are the along-shore averaged velocities. Note that $\overline{U}$, $\overline{V}$, and $\overline{W}$ vary with time if the jet starts to experience

15   finite amplitude perturbations. The baroclinic instability is characterized by a dominance of the former source term, whereas horizontal shear instability by the dominance of the latter. We therefore introduce a *conversion rate ratio* which quantifies the extraction of potential energy relative to the extraction of kinetic energy from the horizontal shear:

$$\mu(t) = \frac{< w'b' >}{< -u'v'\partial_y U >} . \tag{11}$$

We select the stage of exponential growth of KE_y and compute the mean over this time to get a new dimensionless parameter

20    $\mu_0 = \overline{\mu(t)}$, which quantifies the baroclinic or barotropic nature of the energy conversion of the linear instability. The nature of the linear instability appears to have a crucial impact on the wavelength selection. We confirm this result in figure 4b, where all the points of the upper branch correspond to $\mu_0 > 1$ while the lower branch correspond to $\mu_0 < 1$. Hence, these two separated branches are associated with two distinct mechanisms of instability, namely the baroclinic and the barotropic shear instability.

$T_p \simeq -0.4$ seems to act as a threshold between the baroclinic and barotropic modes, as evident in figure 4. Interestingly, we

25   find the same threshold in figure 3b, where we plot the non-linear saturation parameter, ε, with respect to T_p. The non-linear impact of T_p on the saturation of the unstable cross-shore perturbations is striking: all experiments seem to fit on a single curve. From figure 3b we clearly see an abrupt non-linear stabilization of the current when the topographic parameter goes below the threshold value centred around $T_p = -0.4 \pm 0.05$. Below this threshold, the stabilization is so strong that the along-shore current, despite being unstable with $\sigma_m > 0$, is unable to develop significant cross-shore perturbations. These perturbations

30   saturate at a very weak amplitude and hardly affect the along-shore current. For moderate values ($-0.4 < T_p < 0$) the cross-shore perturbations grow until large meanders or coastal eddies are formed, no matter how large the growth rate is. The fact that all the simulations collapse on a single curve is remarkable. This result shows that the topographic parameter T_p is the main parameter that controls the non-linear cross-shore instability.
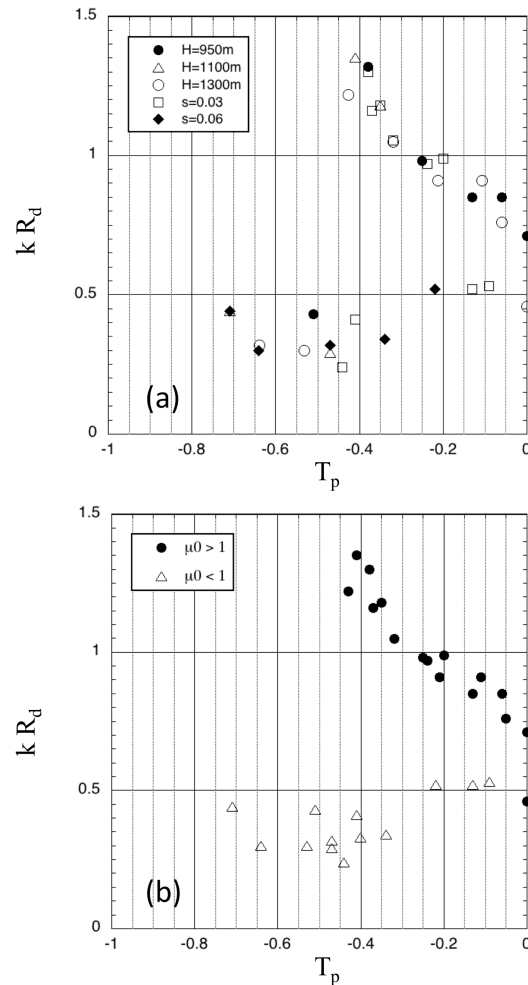
Figure 4. Upper panel (a): most unstable wavenumbers $k_m R_d$ as a function of the topographic parameter T_p for a wide range of bottom slopes ($s = 0 - 6\%$) and water depths ($H = 600 - 5000$ m). Bottom panel (b): same as panel (a), but for different values of the mean conversion rate ratio (μ_0).

We now present a possible interpretation on why $T_p = -0.4$ is the critical value and what changes dynamically at this transition point to explain this result. During the linear stage of the instability, the perturbation grows by extracting energy from the mean flow. When the perturbation becomes large enough, non-linear interactions cause energy to be transfered among modes. Energy transfer is then achieved by the terms of the form $< -u'v'\partial_y u' >$, namely cubic terms in the perturbations, as opposed to the quadratic terms, either $< w'b' >$ or $< -u'v'\partial_y U >$. This non-linear transfer is responsible for the energy cascade in the turbulent regime. If it is dominant then the flow becomes turbulent. The presence of a strong beta effect is known

to prevent these nonlinear interactions and maintain the flow within a wave regime, dominated by Rossby waves (planetary Rossby waves in the case of planetary beta effect and topographic Rossby waves in the present case). The selection between the wave regime and the turbulent regime depends on the size of the eddies with respect to the Rhines scale (Williams and Kelsall, 2015). Usually the Rhines scale is defined in the context of turbulent flow with $L_R = \sqrt{2U_{rms}/\beta}$ where U_{rms} characterizes

5   the intensity of the eddies. Here we propose to substitute $2U_{rms}$ with U_{max}, the jet speed. The rationale is that if eddies form, their $U_{rms} \sim U_{max}$. This gives for the Rhines scale $L_R = \sqrt{U_{max}/\beta_T}$ where β_T is here the *topographic beta* parameter. The typical eddy radius is $R_e = \lambda/4$, where λ is the wavelength of the unstable mode. Using the approximation $kR_d \sim 1$ (figure 3), we have $R_e = \pi R_d/2$. So, T_p can be rewritten as

$$T_p = -\left(\frac{2}{\pi}\right)^2 \left(\frac{R_e}{L_R}\right)^2. \tag{12}$$

10   The discussion on R_e/L_R can now be cast in terms of T_p, with a threshold between the wave and the turbulent regimes of $4/\pi^2 \simeq 0.4$. For $R_e/L_R < 1$, corresponding to $T_p > -0.4$, non-linear interactions can become the leading order term in the energy budget. For $R_e > L_R$, corrreponding to $T_p < -0.4$, the generated eddies are too large compared to the Rhines scale, preventing the non-linear energy transfer to be dominant. The unstable waves stop growing and the flow remains in a wavy regime.

15   However, by using the topographic parameter alone we are not able to distinguish between different non-linear end states when $-0.4 < T_p < 0$. Indeed, figure 4 has shown that at least two distinct instabilites could occur for the same value of T_p, which means that different final states of the flow are possible. This implies that the topographic parameter is not the only dimensionless parameter that controls the unstable regimes of the coastal current above the shelf. We will see shortly, that the vertical aspect ratio $\gamma = H_{jet}/(H - H_{jet})$ is the second parameter to be taken into account.

20   We present in the next two sections the characteristics and parameter space of the different end states identifiable from the non-linear analysis.

5   Quasi-stable, along-shore current (ASC)

We have shown in figure 3b and 4 that below the threshold $T_p = -0.4$ the baroclinic mode is dampened and the non-linear saturation parameter ($\varepsilon \leqslant 0.1$) reaches values at least one order of magnitude smaller than with a larger T_p. This corresponds

25   to a regime in which the buoyant current is quasi-stable, as evidenced from the relative vorticity (figure 5).

From a linear stability perspective, the jet is unstable: waves grow spontaneously from random perturbations, though always very slowly compared to the other regimes. However, the wave growth does not last long and never until the full breaking. The wave amplitudes get saturated at a level small enough to be hardly competing with the background flow, causing the jet to be barely changing in time (figure 5a, c). The flow near the bottom remains very weak (figure 5b, d), both in terms of cross-shore

30   velocity v' or vertical velocity w'. The kinetic energy source for this ASC regime is the extraction from the horizontal shear, with $\mu_0 < 1$.
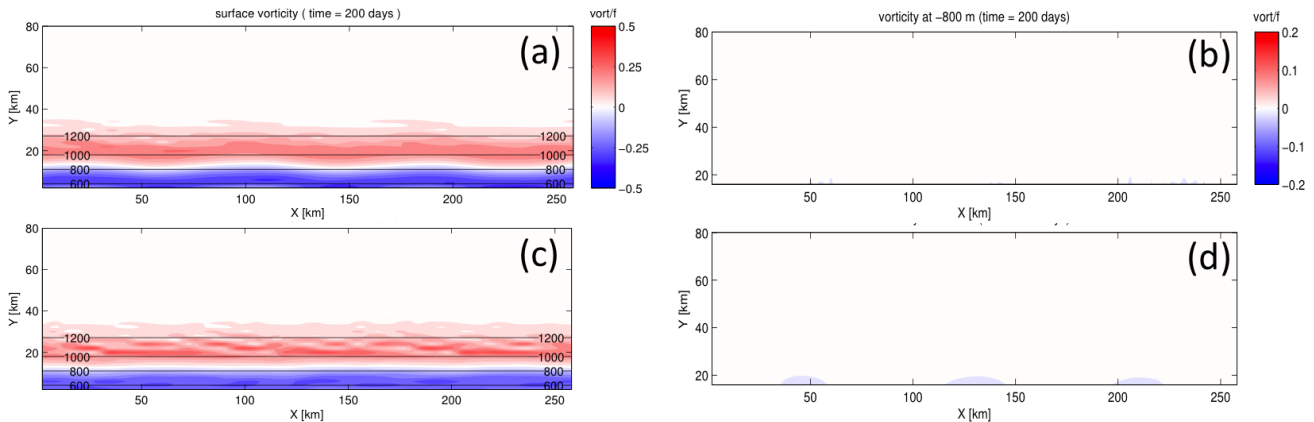
Figure 5. The relative vorticity (ζ/f) at the surface (left panel) and in the deep layer at $z = -800$ m (right panel) for a shelf slope ($s = 3\%$, $T_p = -0.41$) when the aspect ratio parameter is $\gamma \simeq 0.45$ ($H = 800$ m) and the vortex Rossby number is $Ro = 0.25$. The colorbar of the lower layer is magnified by a factor 2.5, in comparison with the upper layer. The panels (a,b) and (c,d) correspond to $t = 200$ days and $t = 400$ days, respectively.

A similar non-linear stabilization was found for coastal fronts and currents with the two-layer laboratory experiments performed by Geheniau et al. (2016). The non-linear stabilization curve as a function of the topographic parameter is less abrupt for these physical experiments, but nevertheless, when the ratio of the bottom slope over the isopycnal slopes goes below $T_0 = s/\alpha < -3$ the non-linear saturation parameter ε does not exceed 0.1. Previous studies have shown that bottom topogra-

5 phy may have a strong impact on the non-linear saturation of an unstable surface flow. For instance, Sutyrin (2001) showed that, in a Gulf Stream-type jet, a very weak bottom slope $s = 0.2\%$ in a deep water case $H = 5000$ m can have a negligible impact on the linear growth of the meanders while significantly impacting the non-linear evolution of the unstable current, the eddy formation, and their subsequent shedding.

As stated in section 2, we have also performed a few runs at the higher grid resolution of $dx = 600$. While this change did

10 not significantly affect the growth rate or the wavelength selection of the most unstable modes, it does affect the level of kinetic energy perturbation in this regime (and consequently ε). The increased resolution of the cross-shore gradient seems to extend the spectrum of unstable modes, leading to a higher amount of energy in the perturbations. Nevertheless, regardless of the grid resolution, the amplitude of the non-linear saturation parameter ε always remains weak in this regime.

6 Coastal meanders and eddy formation

6.1 Coastal eddies regime

The formation of coherent eddies from an unstable coastal current generally results from the pinching off of large meanders. However, these meanders may saturate at an intermediate stage and never lead to the generation of coastal eddies. The value

5 of the non-linear saturation parameter ε cannot distinguish large meanders or coherent eddies, and to perform a quantitative distinction between these two end states we use the vorticity maps. In what follows, we define coherent eddies as vortical structures surrounded with a ring of opposite vorticity, for instance a cyclonic (positive) vorticity ring for an anticyclonic (negative) vorticity core. In other words, when closed contours of zero vorticity appear in the surface vorticity fields coherent eddies are formed in the upper layer, and we will declare the end-state as the coastal eddies regime. In this regime, the eddies

10 systematically detach from the initial location of the coastal current, generating a net cross-shore exchange. As for the buoyant coastal current, the vertical structure of these coherent eddies is baroclinic, with a surface intensification of the vorticity.

However, the vertical structure is not universal and for a similar signature at the surface these coherent eddies could have quite a different structure in the deep layer. Two cases of coastal eddy formation are depicted in figures 6 and 7. In the first case, the eddies have a signature at depth that is partially in phase with the surface (figure 6b, d, f). Dipolar structures are

15 formed in the deep lower layer with a strong vertical alignement of the anticyclonic cores. This is consistent with the tendency for barotropization of the flow induced by the standard baroclinic instability. The anticyclones are more intense and robust at the surface while for the deep layer dipoles the cyclonic vorticity is slightly higher than the anticyclonic one. We have checked for this specific case that the growth of the kinetic energy of the unstable perturbations is mostly explained by the conversion of potential energy because $\mu_0 > 1$. For the second case, the signature of the growing perturbations in the lower layer vorticity

20 (figure 7d, f) is much weaker and the deep layer velocity almost vanishes even if the surface evolution closely resembles the standard baroclinic instability case. This specific case corresponds to a relatively small vertical aspect ratio γ, in other words for deep waters, when baroclinic instability is strongly dampened. Indeed, for this case $\mu_0 < 1$ and the linear stage of instability corresponds to a barotropic shear instability.

Hence, these examples show that two distincts mechanisms of linear instability, namely the baroclinic or the barotropic shear

25 instability, can lead to the same non-linear end state: the formation of coherent eddies in the surface layer which are able to trap water mass in their core and escape from the coast. If we consider only the surface signature of coastal eddies, provided by standard remote sensing measurements such as SST images or SSH maps, we can accurately identify the non-linear coastal eddy regime but hardly make any distinction between the underlying linear instability mechanisms.

6.2 Coastal meanders

30 In contrast with the coastal eddies regime, the formation of coastal meanders correponds to a non-linear stage where the parameter ε reaches a finite value (we chose here $\varepsilon \geq 0.2$) but coherent eddies are never formed. This is a very interesting non-linear regime for unstable coastal currents that has been, as far as we know, rarely studied. The typical evolution of such coastal meanders is depicted in figure 8. The time evolution consists in the growth of the most unstable wave until the
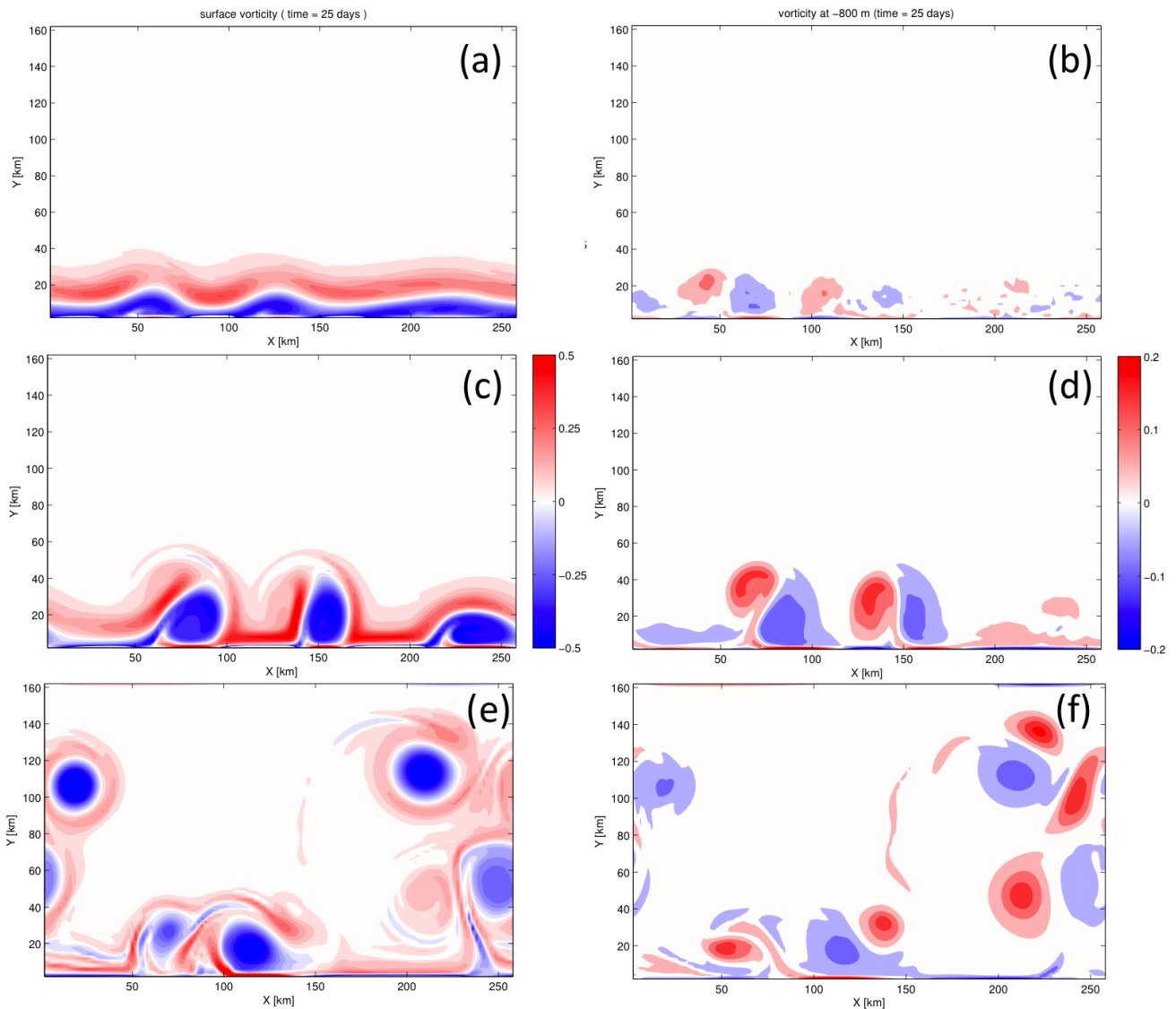
Figure 6. Same as figure 5, but for a flat bottom configuration ($s = 0$, $T_p = 0$) when the aspect ratio parameter is $\gamma = 0.24$ ($H = 1300$ m) and the vortex Rossby number is $Ro = 0.25$. The panels (a,b), (c,d) and (e,f) correspond to $t = 25$, $t = 35$ and $t = 80$ days, respectively.

amplitude saturates at some level. For instance, in figure 8, the non-linear cross shore energy parameter ε goes up to 0.74. The saturation systematically happens before the wave breaks, thus it does not lead to any coherent eddies. The zero vorticity line, which characterizes the maximal velocity of the initial coastal current, may meander but does not pinch off nor close. After saturation, at longer time scales, other unstable waves have grown enough and start to interact with one another. The overall

5   meander pattern evolves slowly and, on the long term, the flow is dominated by waves traveling along the slope, causing a
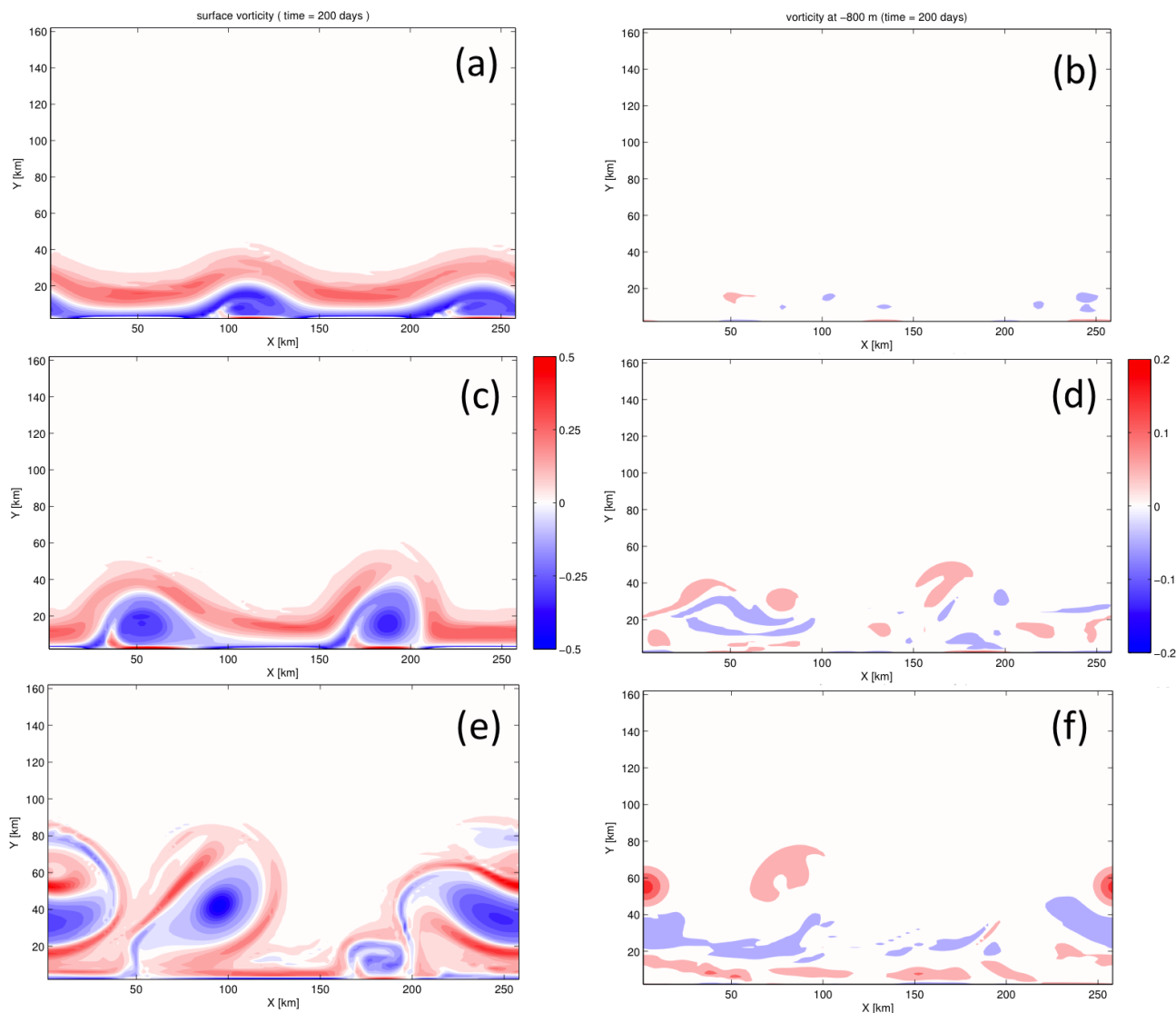
Figure 7. Same as figure 5, but for a shelf slope ($s = 6\%$, $T_p = -0.34$) when the aspect ratio parameter is $\gamma \simeq 0.1$ ($H = 3000$ m) and the vortex Rossby number is $Ro = 0.25$. The panels (a,b), (c,d) and (e,f) correspond to $t = 200$, $t = 280$ and $t = 380$ days, respectively.

loss of the initial meander structure. Note that the non-linear interactions of waves is an interesting process in itself, but the wave interactions are likely over-stimulated in these experiments and quite artificial. The reason is that the periodic condition prevents the wave energy to radiate away along the topography and that somehow bounds the waves to a limited domain, forcing them to interact forever.
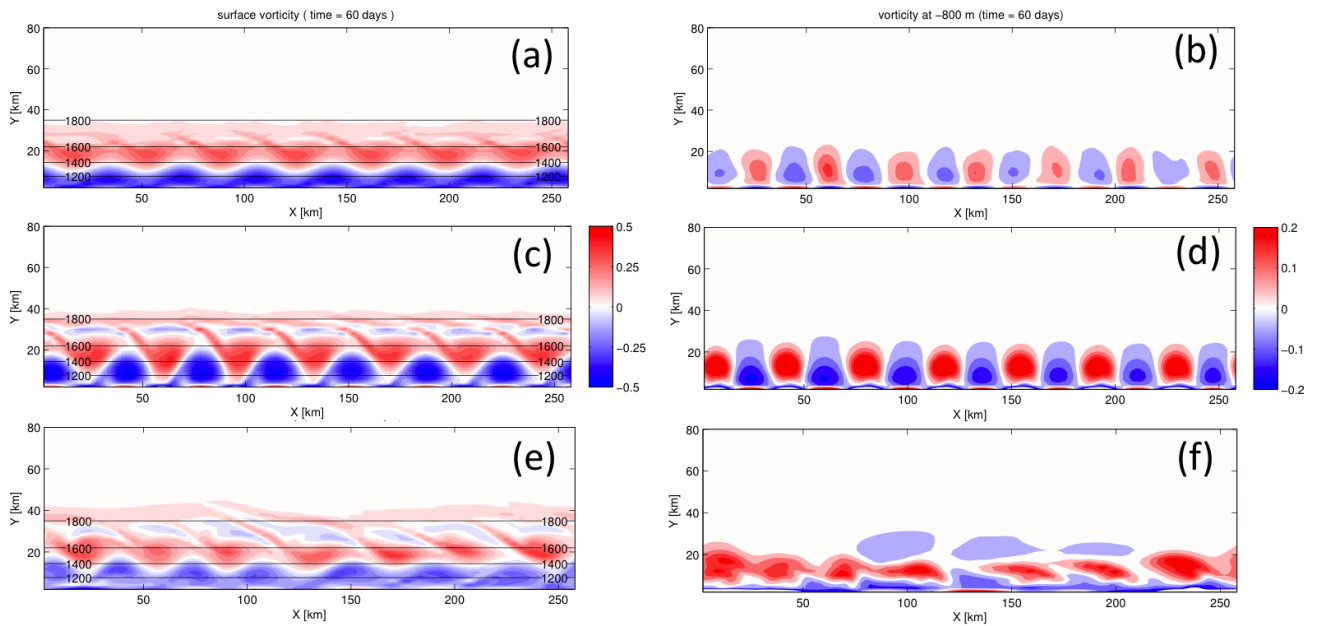
Figure 8. Same as in figure 5, but for a shelf slope ($s = 3\%$, $T_p = -0.32$) when the aspect ratio parameter is $\gamma \simeq 0.24$ ($H = 1300$ m) and the vortex Rossby number is $Ro = 0.25$. The panels (a,b), (c,d) and (e,f) correspond to $t = 60$, $t = 100$ and $t = 150$ days, respectively.

The vertical structure of such coastal meanders is quite different from the coastal eddies regime. The vorticity is never in phase between surface and bottom, but it is rather in phase quadrature (figure 8c,d). The waves have a complex structure in a cross-shore plane (not shown) with several nodal lines but no clear pattern emerges. A key feature of this regime is the bottom intensification of both v' and w'. Such intensification of the cross shore velocities in the deep layer is often a signature of topographic Rossby waves (see e.g. Huthnance (1978) and Brink (1991)). The w' standard deviation ranges from 20 m to 350 m/day, depending on the slope, and reaches its maximum value at the bottom. This bottom intensification would likely be weaker with the presence of bottom friction.

6.3 A two parameter space for meanders and coastal eddy formation

We have shown that T_p is the crucial parameter which controls the final amplitude of the cross-shore perturbations. However, this dimensionless parameter is not the single one that impacts the transition from coherent eddies to coastal meanders. For example, the two distinct dynamical evolutions of the buoyant coastal current depicted in figure 7 and 8 correspond to almost equal values of $T_p \simeq -0.33 \pm 0.01$ while another dimensionless parameter, the vertical aspect ratio $\gamma = H_{jet}/(H - H_{jet})$, differs significantly between these two cases. We found that $\gamma = 0.24$ for the coastal meanders in figure 7 while $\gamma = 0.11$ when coherent eddies are formed (figure 6e). Hence, both T_p and γ should be taken into account, and we propose a two parameter space diagram to predict the various non-linear coastal patterns that may be formed from an unstable buoyant current. Figure
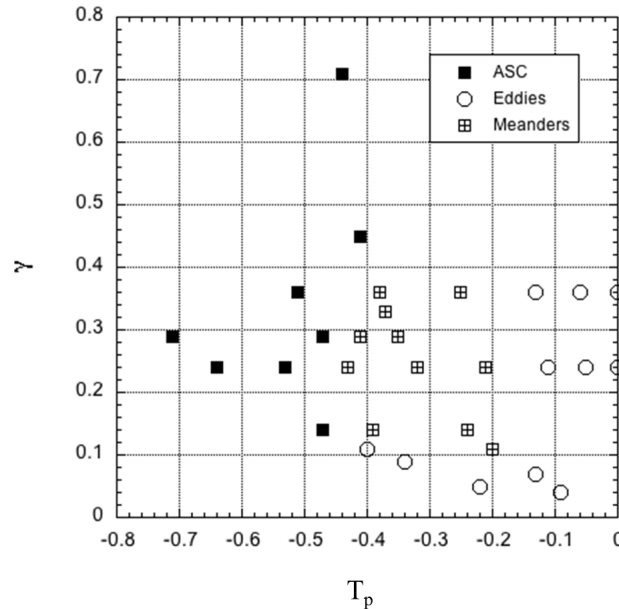
Figure 9. Diagram in the (T_p, γ) parameter space of the various instability regimes: coastal eddies (open circle), coastal meanders (square with cross), and the quasi-stable Along Slope Current (filled square).

9 identifies, in the (T_p, γ) parameter space, the main non-linear regimes between coherent eddies, coastal meanders and the quasi-stable, along-shore current. The formation of coherent coastal eddies occurs when the topographic parameter or the vertical aspect ratio parameter are small ($T_p \gtrsim -0.2$, or $\gamma \lesssim 0.1$), while the emergence of large coastal meanders that remain trapped on the bathymetric slope occurs for a restricted range of values: $\gamma \gtrsim 0.1$ and $-0.4 \lesssim T_p \lesssim -0.2$. Then, for sufficiently negative values of $T_p \lesssim -0.4$ the coastal jet is quasi-stable and the cross-shore perturbations remain asymptotically small.

Note that we have investigated here the range of small and moderate aspect ratio parameter ($\gamma < 0.5 - 0.7$) which corresponds to a surface intensified jet. The limit of large γ corresponds to deeper jets that extend down to the bottom slope. Such cases were investigated by Isachsen (2011) and Brink (2012). They showed that even if the flow is linearly unstable, the peak of eddy kinetic energy is strongly reduced by an increase of the bottom slope.

7 Conclusions

In this paper we have studied the non-linear evolution of an unstable buoyant current, flowing along a coastal slope, for various depths and sloping topographies. The current, kept unchanged, is always linearly unstable. We determined the properties of the linear instability (growth rate, wavelength) from the direct integration of the primitive equations forward in time. The properties of the linear stage (the exponential growth) match published results (Poulin et al., 2014) with, in particular, two unstable branches in the stability diagram: a branch associated with baroclinic instability, where the wavelength of the most

unstable mode decreases as slope increases, and a branch associated with horizontal shear instability, where the wavelength is independent of the slope. The advantage of integrating the primitive equations forward in time is to go beyond the linear stage, and to reveal the full non-linear evolution. The non-linear regime clearly adds richness and cannot be simply predicted by the linear analysis. Indeed, we found three non-linear end states correponding to coherent eddies, coastal meanders or quasi-stable

5 jet, while the linear analysis predicted only two types of instability. These distinct non-linear end states correpond to specific patterns that could be easily identified from remote sensing observations of the ocean surface such as high resolution SST images. We show in figure 10 the typical signature of these three non-linear regimes on the surface temperature field obtained in our simulations (we plot here the results from the high resolution cases to give a better representation of the SST pattern at meso- and submeso-scales). The initial temperature distribution is given by equation (3) with a warm along shore anomaly

10 attached to the coast. The generation of closed patches of warm waters (figure 10a) are associated here with coherent eddies, while the undulations of the warm coastal area (figure 10b) are associated with the large coastal meanders. In the third regime, the quasi-stable along shore current, small wavy patterns are visible on the SST front. This in an interesting difference in comparison with the low resolution (2 km) cases, because it shows the emergence of submeso-scale structures, generated from the initial instability. While these structures are not visible in the low resolution cases, they never reach a finite amplitude, so

15 their emergence does not change the main results presented in this paper. It confirms that the flow is linearly unstable, but the amplitude of the unstable perturbations hardly affects the along shore current.

The most interesting finding of this study is that T_p is the key parameter that controls the amplitude of the unstable cross-shore perturbations, defined as the ratio of the cross-shore contribution to the kinetic energy to the total kinetic energy. The collapse of experimental points (ε, T_p) on a single curve (figure 3) is remarkable, given the wide diversity of cases. Moreover,

20 we have checked that complementary points, corresponding to different jet velocities, also collapse on the same curve. This confirms that the ratio T_p of the topographic Rossby wave phase speed over the jet speed is the generic dimensionless parameter which controls the non-linear cross-shore patterns of the buoyant coastal current. This parameter is proportional to the topographic slope, and therefore it can be intepreted as a measure of the slope's relative importance. Indeed, even though a slope is dimensionless, it does not adequately quantify whether the topography is steep or gentle in a dynamical sense, while

25 T_p does. For sufficiently negative values of T_p the current is quasi-stable: even if small scale perturbations could grow, their amplitude would remain small, and thus the mean current follows the along-shore bathymetry and does not lead to any significant cross-shore transport. $T_p \simeq 0.4$ emerges as an important threshold between an quasi-stable, along-shore jet on one hand, and a non-linear, strongly topographically controlled flow on the other hand.

We have also shown that in addition to the topographic parameter T_p, another dimensionless parameter, the vertical aspect

30 ratio of the buoyant current $\gamma = H_{jet}/(H - H_{jet})$, controls the formation of coherent eddies, which may escape from the coast, or the non-linear meanders, that remain attached to the coast. As far as we know this is the first time that an explicit parameter space is provided for the emergence of coastal eddies or meanders from an unstable buoyant current. This (T_p, γ) parameter space might be quite convenient for real coastal currents because approximated values for these two dimensionless parameters could be easily estimated with a minimal number of in-situ measurements. For instance, hydrographic sections are sufficient

35 to quantify the first baroclinic deformation radius R_d, the maximum geostrophic velocity V_{max}, and the vertical extent H_{jet}
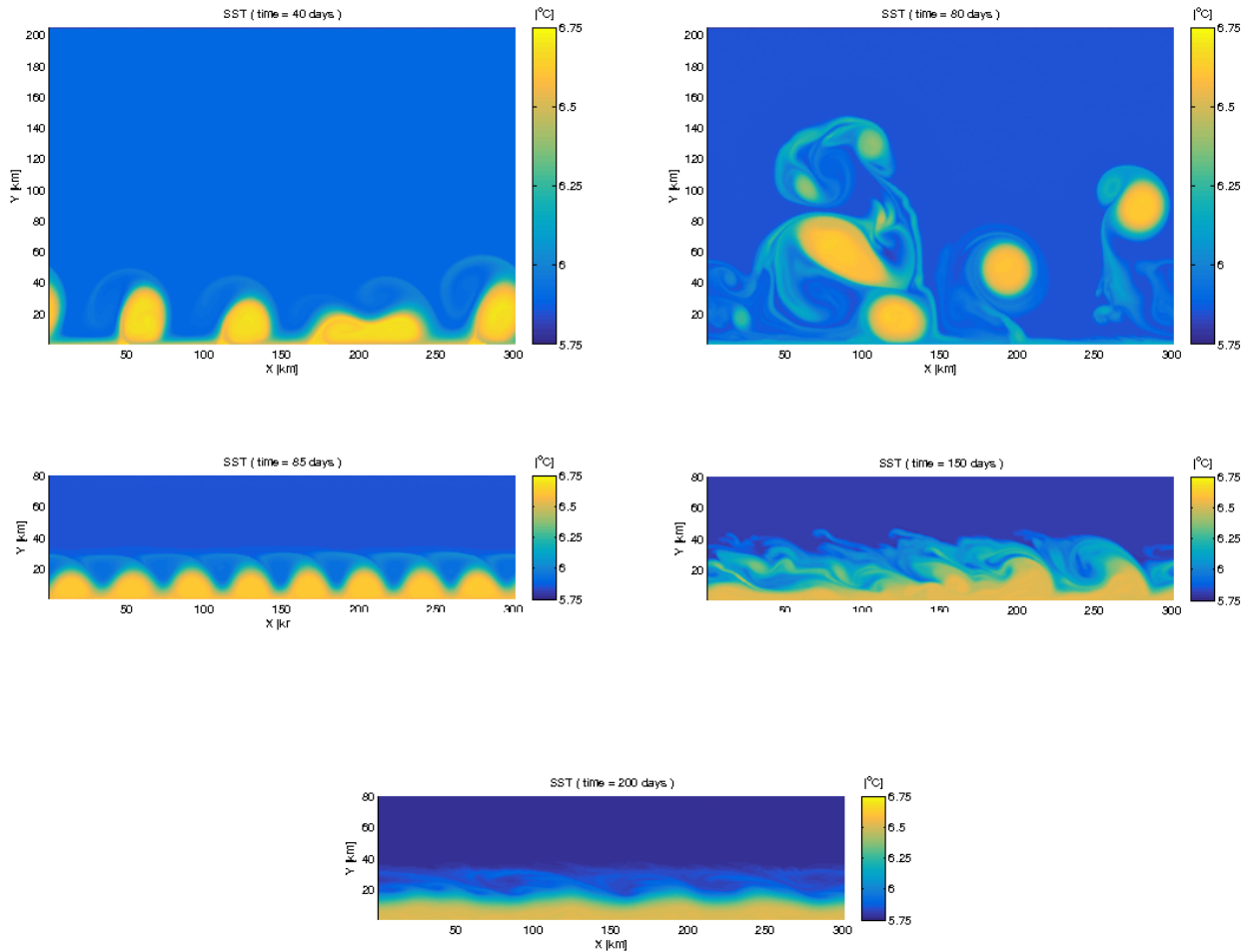
Figure 10. Snapshots of SST for the coastal eddies regime (top panels), the coastal meanders regime (central panels) and the quasi-stable along-shore current regime (bottom panel). The details of these simulations are presented in table 2.

of the surface current. Then, a standard bathymetric data set will provide a correct averaging of the bottom slope s in the cross shore direction. If we consider the coastal Bransfield Current, which inspired the setup of the model used in this study and which has been extensively studied by Savidge and Amft (2009), Sangrá et al. (2011), Poulin et al. (2014) and Sangrá et al. (2017), we get from the combination of numerous CTD stations and ADCP data the following values: $R_d \simeq 10$ km, $U_{max} \simeq 35$ cm s^{-1}, $H_{jet} \simeq 250$ m, and $H \simeq 900 - 1000$ m, while the maximum shelf slope is around $s \simeq 15\%$ (Poulin et al., 2014). We

then obtain $\gamma = 0.3 - 0.4$ and a strongly negative value for the topographic parameter, $T_p \simeq -6$. Therefore, according to our study, the Bransfield Current flows over a very steep shelf slope and should correspond to a quasi-stable, along-shore current. This non-linear analysis extends, to a fully stratified case, the linear stability analysis performed by Poulin et al. (2014) with a two-layer shallow-water model. Such a result is in good agreement with the various drifter paths (Zhou et al., 2002; Poulin

5   et al., 2014), which show that the Bransfield Current does not exhibit any significant meanders along the steep coastal shelf and seems to be relatively stable in the summer months.

This work emphasizes the limitations of linear stability analysis to classify eddy formation, because it does not account for the non-linear saturation which is predominant for large negative T_p values. Nevertheless, we are aware that this work is a first step of a more thorough analysis. The idealized configuration tested here accounts only for initial-value problems, with a

10   weak white noise on the velocity field. This is of course an artificial situation compared to the continually forced circulation in the real ocean. Moreover, the geometry used here may constrain the results in a number of ways. We performed a few tests with different initial velocities and found that there was no effect on the different non-linear end state, but a different jet structure and/or a different distance from the coast are very likely to affect the results, since the initial vertical vorticity would be different. Also, given that the velocity of the topographic Rossby waves is proportional to the width of shelf, this parameter

15   should be also taken into account. The width of the shelf might become particularly important for very steep cases (steeper than the ones tested here), when it becomes comparable with the jet width. Finally, the effect of the bottom friction is here neglected since we focused on the inviscid dynamics and set the friction to zero to prevent a slow down of the jet during the initial period of integration. The sensitivity of the results presented here to these other parameters will be investigated in a future study.

Appendix A: Estimate of the first baroclinic deformation radius

20   For a continuous stratification $\rho(z)$, the linear eigenmodes and the corresponding deformation radius are given by the equation:

$$-\partial_z \left(\frac{\rho_0 f^2}{g} \frac{\partial_z \psi_n}{\partial_z \rho} \right) = \partial_z \left(\frac{f^2}{N^2(z)} \partial_z \psi_n \right). \tag{A1}$$

With the appropriate boundary conditions, it returns

$$-\frac{\psi_n}{R_{d,n}^2} \partial_z \psi_n(z=0) \;\; = \;\; \partial_z \psi_n(z=-H) \;\; = 0.$$

where $R_{d,i}$ are the deformation radius associated to the baroclinic modes $n = 1, 2, ...$ This equation is identical to equation

25   (5.204) in Vallis (2006). We plot in the figure A1 the characteristic density profile obtained in the center of the coastal jet (figure A1a) and an example of the vertical profile of the first baroclinic eigenmode (figure A1b).

The first baroclinic deformation radius corresponding to this stratification is $R_{d,1} = 6.1$ km (this Rossby radius is denoted R_d in the present study). This value is smaller than the typical width of the jet $L = 10$ km. According to the figure A1c the Rossby radius R_d increases with the water depth H. In other words, the Burger number Bu decays when the aspect ratio

30   parameter γ increases. For the range of parameters used in this study the Burger number remains small.
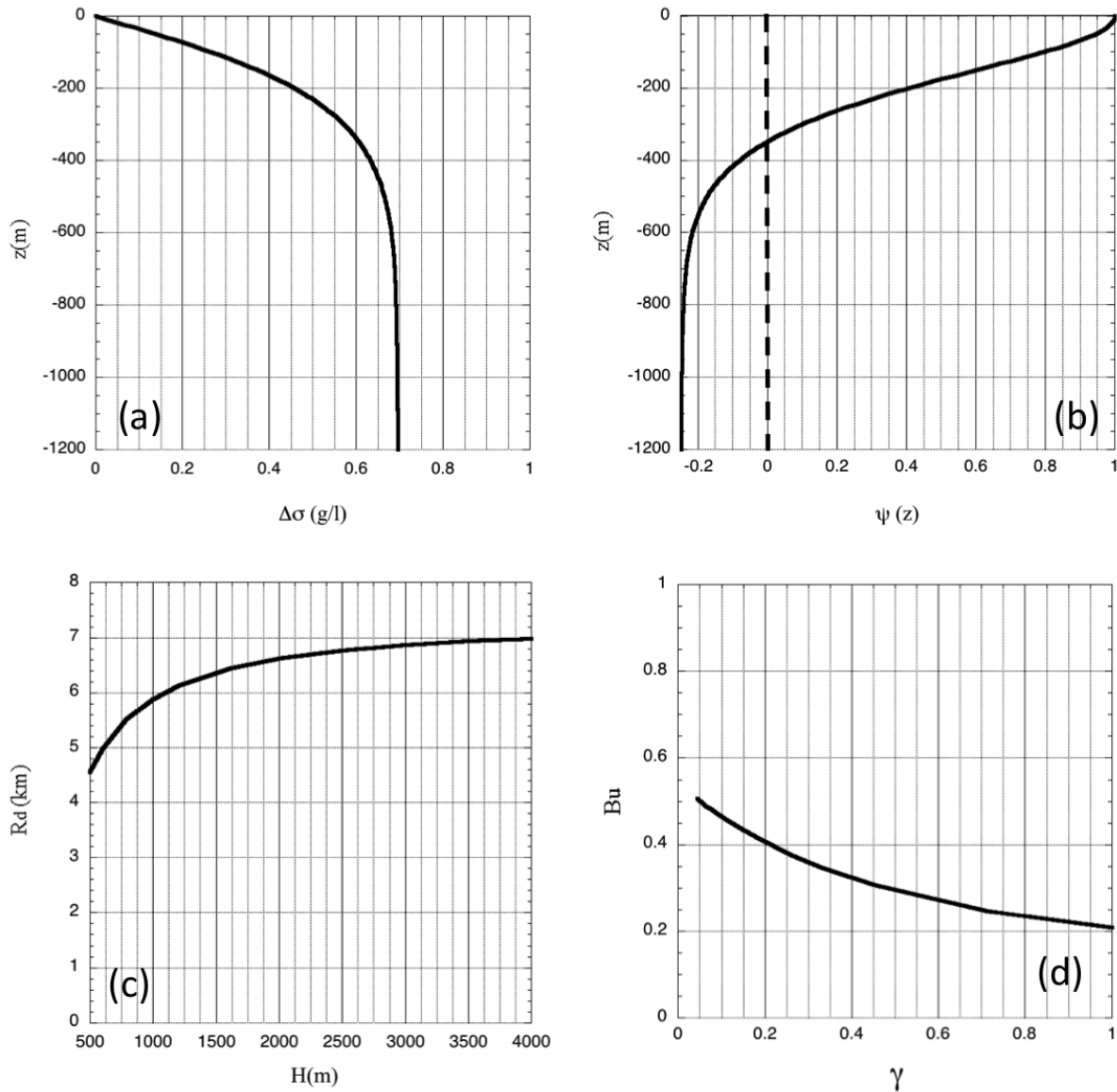
Figure A1. Vertical profile of the potential density anomaly $\Delta\sigma(z)$ (a) and the vertical structure of the first baroclinic eigenmode (b) computed in the center of the coastal current $y = D$ for a water depth $H = 1200$ m. The evolution of the first baroclinic deformation radius R_d is plotted in panel (c) as a function of the water depth H. Panel (d) shows the evolution of the corresponding Burger number $Bu = (R_d/L)^2$ as a function of $\gamma = H_{jet}/(H - H_{jet})$.

Acknowledgements. This work was funded by the ANR Astrid Project SYNBIOS (ANR 11 ASTR 014 01).

References

Birol, F., Cancet, M., and Estournel, C.: Aspects of the seasonal variability of the Northern Current (NW Mediterranean Sea) observed by altimetry, J. Mar. Syst., 81, 297–311, 2010.

Björk, G., Gustafsson, B., and Stigebrandt, A.: Upper layer circulation of the Nordic seas as inferred from the spatial distribution of heat and freshwater content and potential energy, Polar Res., 20, 161–168, 2001.

Blumsack, S. and Gierasch, P.: Mars - The effects of topography on baroclinic instability, J. Atmos. Sci., 29, 1081–1089, 1972.

Brink, K. H.: Coastal-trapped waves and wind-driven currents over the continental shelf, Annu. Rev. Fluid. Mech., 23, 389–412, 1991.

Brink, K. H.: Baroclinic instability of an idealized tidal mixing front, J. Mar. Res., 70, 661–688, 2012.

Debreu, L., Marchesiello, P., Penven, P., and Cambon, G.: Two-way nesting in split-explicit ocean models: algorithms, implementation and validation, Ocean Model., 49-50, 1–21, 2011.

Eden, C. and Boning, C.: Sources of eddy kinetic energy in the Labrador Sea, J. Phys. Oceanogr., 32, 3346–3363, 2002.

Geheniau, N., Pennel, R., and Stegner, A.: Non-linear stabilization of coastal fronts and currents by a sloping bathymetry: laboratory experiments, in prep., 2016.

Gula, J. and Zeitlin, V.: Instabilities of shallow-water flows with vertical shear in the rotating annulus. Modelling Atmospheric and Oceanic flows: insights from laboratory experiments and numerical simulations, Amer. Geophys. Union, edited by T. von Larcher and P. Williams, ISBN 978-1-118-85593-5, 2014.

Gula, J., Molemaker, M., and McWilliams, J.: Submesoscale cold filaments in the Gulf Stream, J. Phys. Oceanogr., 44, 2617–2643, 2014.

Gula, J., Molemaker, M., and McWilliams, J.: Gulf Stream dynamics along the southeastern US seaboard, Journal of Phys. Oceanogr., 45, 690–715, 2015.

Hátún, H., Eriksen, C., and Rhines, P.: Buoyant eddies entering the Labrador Sea observed with gliders and altimetry, J. Phys. Oceanogr., 37, 2838–2854, 2007.

Huthnance, J.: On coastal trapped waves: analysis and numerical calculation by inverse iteration, J. Phys. Oceanogr., 8, 74–92, 1978.

Isachsen, P. A.: Baroclinic instability and eddy tracer transport across sloping bottom topography: how well does a modified Eady model do in primitive equation simulations?, Ocean Model., 39, 183–199, 2011.

Knox, J. A.: Inertial instability, Encycl. Atmos. Sci., pp. 1004–1013, edited by J. R. Holton, J. A. Curry and J. A. Pyle, 2003.

Lozier, M. and Reed, M.: The influence of topography on the stability of shelfbreak fronts, J. Phys. Oceanogr., 35, 1023–1036, 2005.

Lozier, M., Reed, M., and Gawarkiewicz, G.: Instability of a shelfbreak front, J. Phys. Oceanogr., 32, 924–944, 2002.

Mechoso, C.: Baroclinic instability of flows along sloping boundaries, J. Atmos. Sci., 37, 1393–1399, 1980.

Millot, C.: Circulation in the western Mediterranean Sea, J. Mar. Syst., 20, 423–442, 1999.

Mysak, L.: On the stability of the California Undercurrent off Vancouver Island, J. Phys. Oceanogr., 7, 904–917, 1977.

Mysak, L., Muench, R. D., and Schumacher, J. D.: Baroclinic Instability in a downstream varying channel: Shelikof Strait, Alaska, J. Phys. Oceanogr., 11, 950–969, 1981.

Obaton, D., Millot, C., d'Hières I., G. C., and Taupier-Letage: The Algerian Current: comparisons between in situ and laboratory data sets, Deep Sea Res., 47, 2159–2190, 2000.

Pedlosky, J.: Geophysical Physical Dynamics, Springer New York, 1987.

Pennel, R., Stegner, A., and Béranger, K.: Shelf impact on buoyant coastal current instabilities, J. Phys. Oceanogr,, 42, 39–61, 2012.

Penven, P., Debreu, L., Marchesiello, P., and McWilliams, J. C.: Evaluation and application of the ROMS 1-way embedding procedure to the central california upwelling system, Ocean Model., 12, 157–187, 2006.

Phillips, N. A.: Energy transformations and meridional circulation associated with baroclinic waves in a two-level, quasi-geostrophic model, Tellus, 6, 273–286, 1954.

5   Pickart, R. S., Torres, D., and Fratantoni, P.: The East Greenland Spill Jet, J. Phys. Oceanogr., 35, 1037–1053, 2005.

Plougonven, R. and Zeitlin, V.: Nonlinear development of inertial instability in a barotropic shear, Phys. Fluids, 21, 2009.

Poulin, F. and Flierl, G.: The influence of topography on the stability of jets, J. Phys. Oceanogr., 35, 811–825, 2005.

Poulin, F., Stegner, A., Arencibia, M. H., Diaz, A. M., and Sangrá, P.: Steep Shelf Stabilization of the Coastal Bransfield Current: Linear Stability Analysis, J. Phys. Oceanogr., 44, 714–732, 2014.

10 Puillat, I., Taupier-Letage, I., and Millot, C.: Algerian eddies lifetime can near 3 years, J. Mar. Syst., 31, 245–259, 2002.

Riandey, V., Champalbert, G., Carlotti, F., Taupier-Letage, I., and Thibault-Botha, D.: Zooplankton distribution related to the hydrodynamic features in the Algerian Basin (western Mediterranean Sea) in summer 1997, Deep-Sea Res., 52, 2029–2048, 2005.

Sammari, C., Millot, C., and Prieur, L.: Aspects of the seasonal and mesoscale variabilities of the Northern Current in the western Mediterranean Sea inferred from the PROLIG-2 and PROS-6 experiments, Deep Sea Res. Part I: Oceanographic Research Papers, 42, 893–917,
15   1995.

Sangrá, P., Gordo, C., Arencibia, M. H., Marrero-Díaz, A., Rodríguez-Santana, A., Stegner, A., Martínez-Marrero, A., Pelegrí, J. L., and Pichon, T.: The Bransfield Current System, Deep Sea Res., 58, 390–402, 2011.

Sangrá, P., Stegner, A., Arencibia, M. H., Marrero-Díaz, A., Salinas, C., Aguiar-González, B., and Henríquez-Pastene, C.: The Bransfield gravity current, Deep Sea Res., in press, 2017.

20 Savidge, D. and Amft, J.: Circulation on the west Antarctic Peninsula derived from 6 years of shipboard ADCP transects, Deep Sea Res., 56, 1633–1655, 2009.

Shchepetkin, A. F. and McWilliams, J. C.: A method for computing horizontal pressure-gradient force in an oceanic model with a nonaligned vertical coordinate, J. Geophys. Res., 108, 1978–2012, 2003.

Shchepetkin, A. F. and McWilliams, J. C.: The regional oceanic modeling system (roms): a split-explicit, free-surface, topography-following-
25   coordinate oceanic model, Ocean Model., 9, 347–404, 2005.

Stewart, A. L. and Thompson, A. F.: Connecting Antarctic cross-slope exchange with Southern Ocean overturning, J. Phys. Oceanogr., 43, 1453–1471, 2013.

Sutyrin, G.: Effects of a topographic slope on the β-drift of a baroclinic vortex, J. Mar. Res., 59, 977–989, 2001.

Vallis, G. K.: Atmospheric and Oceanic Fluid Dynamics, Cambridge University Press, Cambridge, U.K., 2006.

30 Williams, P. and Kelsall, C.: The dynamics of baroclinic zonal jets, J. Atmos. Sci., 72, 1137–1151, 2015.

Zhou, M., Niiler, P., and Hu, J.: Surface currents in the Bransfield and Gerlache Straits, Antarctica, Deep-Sea Res., 49, 267–280, 2002.

Table 1. Parameter space of the experiments performed with a 2 km grid resolution, where s is the topographic slope (%), H the water depth below the maximum current velocity (m), $|T_p|$ is the absolute value of the topographic parameter, γ is the vertical aspect ratio, $\sigma_m R_d / V_{max}$ is the dimensionless growth rate, ε is the non-linear saturation parameter, $k_m R_d$ is the most unstable wavenumber and μ_0 the averaged conversion rate ratio.

s (%)	H	$|T_p|$	γ	$\sigma_m R_d / U_{max}$	ε	$k_m R_d$	μ_0	regime
0	950	0.00	0.36	0.030	1.11	0.71	1.43	eddies
0	1300	0.00	0.24	0.027	1.06	0.46	1.26	eddies
0.5	950	0.06	0.36	0.029	1.35	0.85	1.73	eddies
0.5	1300	0.05	0.24	0.025	1.28	0.76	1.42	eddies
1	950	0.13	0.36	0.023	1.14	0.85	1.61	eddies
1	1300	0.11	0.24	0.021	1.27	0.91	1.44	eddies
2	950	0.25	0.36	0.010	0.60	0.98	1.51	meanders
2	1300	0.21	0.24	0.014	0.95	0.91	1.32	meanders
3	600	0.44	0.71	0.001	0.05	0.24	0.10	ASC
3	800	0.41	0.45	0.002	0.01	0.41	0.11	ASC
3	950	0.38	0.36	0.002	0.19	1.30	4.32	meanders
3	1000	0.37	0.33	0.005	0.29	1.16	2.12	meanders
3	1100	0.35	0.29	0.008	0.63	1.18	2.27	meanders
3	1300	0.32	0.24	0.012	0.74	1.05	1.44	meanders
3	2000	0.24	0.14	0.011	0.97	0.97	1.43	meanders
3	2500	0.20	0.11	0.010	1.11	0.99	1.06	meanders
3	4000	0.13	0.07	0.005	0.88	0.52	0.45	eddies
3	6000	0.09	0.04	0.008	0.93	0.53	0.52	eddies

s (%)	H	$|T_p|$	γ	$\sigma_m R_d$ / U_{max}	ε	$k_m R_d$	μ_0	regime
3.5	1100	0.41	0.29	0.003	0.19	1.35	1.78	meanders
4	950	0.51	0.36	0.001	0.01	0.43	0.07	ASC
4	1100	0.47	0.29	0.002	0.03	0.29	0.34	ASC
4	1300	0.43	0.24	0.004	0.46	1.22	1.92	meanders
5	1300	0.53	0.24	0.002	0.04	0.30	0.52	ASC
5	2000	0.39	0.14	0.005	0.55	1.12	1.13	meanders
6	1100	0.71	0.29	0.002	0.01	0.44	0.05	ASC
6	1300	0.64	0.24	0.002	0.01	0.30	0.08	ASC
6	2000	0.47	0.14	0.003	0.26	0.32	0.34	ASC
6	2500	0.40	0.11	0.004	0.44	0.33	0.33	eddies
6	3000	0.34	0.09	0.005	0.97	0.34	0.32	eddies
6	5000	0.22	0.05	0.009	0.81	0.52	0.45	eddies

Table 2. Same as table 1, but for the high resolution cases (600 m grid resolution).

s (%)	H	$|T_p|$	γ	$\sigma_m R_d$ / U_{max}	ε	$k_m R_d$	μ_0	regime
0	1300	0.00	0.24	0.027	1.28	0.52	2.44	eddies
3	800	0.41	0.45	0.002	0.06	0.58	1.76	ASC
3	1300	0.32	0.24	0.012	0.74	1.03	3.08	meanders